Editors' Suggestion

# Abnormal response of $Ti_3SiC_2$ to high strain-rate loading

Maxim Sokol,[1] Sergey Kalabukhov,[2] Eugene Zaretsky,[3] and Michel W. Barsoum[1,*]
[1]Department of Materials Science & Engineering, Drexel University, Philadelphia, Pennsylvania 19104, USA
[2]Department of Materials Engineering, Ben-Gurion University of the Negev, P.O. Box 653, Beer-Sheva 8410501, Israel
[3]Department of Mechanical Engineering, Ben-Gurion University of the Negev, P.O. Box 653, Beer-Sheva 8410501, Israel

(Received 27 March 2019; published 21 June 2019)

Herein, we report on the response of the MAX phase, $Ti_3SiC_2$, to shock wave compression at strain rates above $10^4$ $s^{-1}$. The shock response was determined by measuring the rear, free surface, and velocity of samples—subjected to impact by high-velocity projectiles launched by a gas-gun—using interferometry. The effects of temperature and sample thickness on the dynamic yield and dynamic tensile (spall) strengths were studied. The most important result of this work is the unique dual nature, at high strain rates, of the response of $Ti_3SiC_2$, in that it is reminiscent of both metals and ceramics. For low-energy impacts, the elastic response is reminiscent of ductile metals. However, for high-energy impacts, it performed like a hard ceramic with quite high work hardening rates. In other words, $Ti_3SiC_2$ behaves like nothing before it and thus must reflect its nanolayered structure. This work not only provides results on the dynamic mechanical properties of $Ti_3SiC_2$, but is a critical first step toward understanding the response of ripplocations in layered solids to high strain rates.

DOI: 10.1103/PhysRevMaterials.3.063610

## I. INTRODUCTION

The $M_{n+1}AX_n$ (MAX) phases are ternary, thermodynamically stable nanolayered hexagonal carbides and nitrides, where $M$ is an early transition metal, $A$ is a group A element (mostly from groups 13 and 14), and $X$ is C and/or N [1]. To date, there are over 155 known MAX phases, which can be further categorized by their $n$ value as "211s" for $M_2AX$ ($n = 1$), "312s" for $M_3AX_2$ ($n = 2$), and "413s" for $M_4AX_3$ ($n = 3$). [2]. The MAX phases combine some of the more attractive properties of ceramics and metals. They are all metallic-like conductors—in some cases, their conductivities are higher than those of their pure $M$ element [3,4]. They are relatively soft (Vickers hardness range from 1.4 to 8 GPa), plastic at high temperatures, and damage-tolerant [5,6].

In layered crystalline solids, such as graphite, mica, the MAX phases, and many others, basal dislocations have long been considered to be the operational micromechanism for their deformation [7–10]. However, in many other fields, where the layers can be either crystalline and/or amorphous (i.e., geology [11,12], wood [13], playing cards [14], laminated composites, etc.), basal dislocations (BDs) have never been invoked. Instead, it has been assumed that a buckling mechanism, which typically results in kink band formation, is operative. Moreover, the fact that many crystalline layered solids fail in compression—but not tension—by forming kink bands, such as those seen in other fields, suggests that maybe BDs were not the main operational micromechanism in the deformation of layered solids.

Kushima *et al.* [15] coined the word "ripplocation" [Fig. 1(a)] for a near surface defect in Van der Waals solids. Using density functional theory (DFT), they demonstrated that ripplocations were fundamentally different from dislocations by showing that two ripplocations of the same polarity attracted, in contradistinction to two dislocations of the same sign that repel [Fig. 1(a)]. Shortly thereafter, we used molecular dynamics (MDs) on graphite and transmission electron microscopy (TEM) observations on $Ti_3SiC_2$ after spherical nanoindentation [16] to extend the idea to most layered solids, and we introduced the idea of a bulk ripplocations [Fig. 1(b)] [14,16–21]. Our MD calculations showed that ripplocations, unlike dislocations, have no polarities and are surprisingly mobile in graphite even at 10 K. In the nanoindentation experiments, we also showed extremely high hardening rates. Along the same lines, a hallmark of deformation by ripplocations is the strong effect of confinement on yield points [8,22–25], a feature that was not easily reconciled with basal dislocations [18].

Single ripplocations are probably as rare as isolated dislocations. Instead we showed that layered solids require an inhomogeneous state of stress [e.g., Fig. 1(c)] and that the response depends on the relative size of the perturbation or applied strain field, $\Lambda$, relative to the thicknesses of the individual sheets, $\tau$. If $\Lambda \approx \tau$, the layers respond by nucleating evenly spaced ripplocation boundaries (RBs) that propagate, wavelike, from the source of the stress, as shown in Fig. 1(c) for plastic cards, thin steel sheets, and graphite. The movies/simulations shown in Ref. [14] are quite instructive in that they show that the process is one of confined buckling. RBs are defined as the locus of points joining the highest curvature in each layer [19]. In this case, the wavelengths of the RBs, $\lambda_{RB}$, are of the order of $\Lambda$ and the RBs [26]. However, if $\Lambda \gg \tau$, the response is quite complex wherein a large number of RBs interact together in quite complex ways, as shown in MD simulations that can be found in Refs. [16,17]. In all cases, however, upon removal of the stress, the system reverts back to its pristine state, i.e., the process is fully reversible. This reversibility, however, has a limit; once the

*Author to whom all correspondence should be addressed: barsoumw@drexel.edu

 

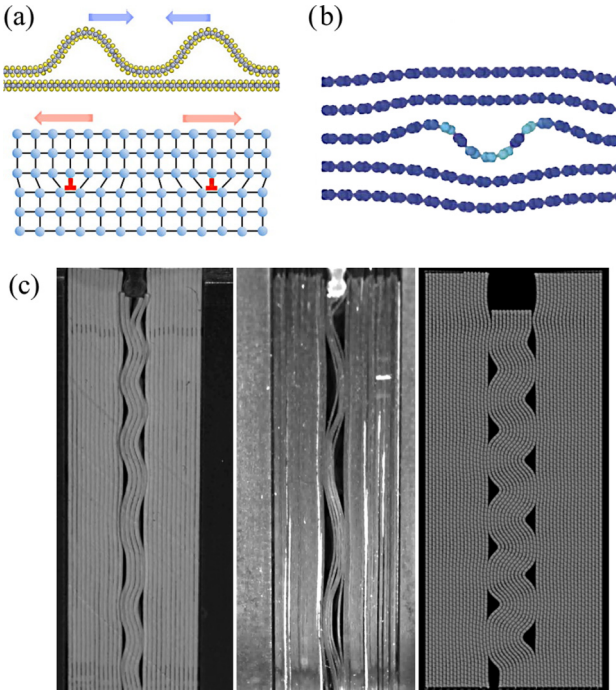


FIG. 1. (a) Comparison between edge dislocations and ripplocations in a generic lattice. Both deformation micromechanisms allow the relative movement of one plane of atoms over another. However, in the case of dislocation, there is only in-plane strain, and climb is required to deform out of plane. Additionally, two dislocations of the same sign repel, but two ripplocations of the same sign attract [15]. (b) For ripplocations, *c*-axis strain is embedded, and can be observed in MD simulations of graphite. (c) Snapshots of ripplocation boundaries formed when a cylindrical indenter is loaded edge-on into, from left to right, plastic cards, thin steel sheets, and graphite (MD simulation). Images adapted with permission from Refs. [14,15,17].

amplitudes of the RBs are high enough, they cause quasibrittle failure of polycrystalline solids or kink bands in single crystals [27–29].

Somewhat surprisingly, and even though the MAX phases have attracted much attention for over two decades, little of that attention was dedicated to understanding their response to dynamic loading environments. As far as we are aware, apart from the work of Bhattacharya *et al.*, Naik *et al.*, and Shannahan *et al.*—who tested some MAX phases at maximum strain rates of $\approx 10^3\ s^{-1}$—and by Jordan *et al.* on the Hugoniot measurements of $Ti_3SiC_2$, there is little else on the subject in the literature [30–34]. The purpose of this work was to study the response of one of the most studied of the MAX phases, viz. $Ti_3SiC_2$, to shock experiments at strain rates as high as $10^4\ s^{-1}$. To that effect, its dynamic compressive and tensile (spall) strengths were tested using Velocity Interferometer System for Any Reflector (VISAR) [35] planar impact (shock) experiments as a function of sample thickness and temperature, which ranged from 300 to 1200 K [35].

## II. MATERIALS AND METHODS

Polycrystalline $Ti_3SiC_2$ samples were prepared by ball-milling a 1.95:1:1 stoichiometric mixture of TiC (325 mesh, 99%, Alfa Aesar), Si (325 mesh, 99.5%, Alfa Aesar), and Ti (325 mesh, 99%, Alfa Aesar) powders for 24 h in a polyethylene jar using zirconia milling balls. The mixed powders were poured into a boron nitride-coated graphite die. The die was placed in a graphite element heated hot press (HP) and pre-compacted to 5 MPa. The die was then heated at a rate of 400 °C/h to a maximum temperature of 1550 °C under a uniaxial load corresponding to a stress of 25 MPa. This temperature and pressure were maintained for 4 h before cooling down at a rate of 400 °C/h. The HPed samples' surfaces were ground to remove any surface boron nitride, graphite, and/or carbide residues before further preparation for dynamic testing.

The bulk polycrystalline $Ti_3SiC_2$ sample was cut with a diamond saw into ~3 mm thick, $11 \times 11\ mm^2$ squares. The squares were polished down to the required nominal thicknesses (0.5, 1, 2, or 3 mm) and 1 arc min parallelism. To enhance the reflection of the laser light, on one surface of the square samples a micron layer of gold was vacuum-deposited.

For microstructure analysis the sample was mounted, ground, polished, and etched for 2–3 s by a 1:1:1 part solution of hydrofluoric acid (48%, Sigma Aldrich, St. Louis, MO), nitric acid (68%, Alfa Aesar, Ward Hill, MA), and water. The microstructures were imaged in a scanning electron microscope, SEM (XL30, FEI, Hillsboro, OR). The SEM images were processed using ImageJ software to obtain the average grain size [36]. Up to 10 images were analyzed, and several hundreds of individual grains were examined. The average and standard deviations of the grain size, determined from the SEM images, were found to be $\approx 50 \pm 13\ \mu m$ [Fig. 2(a)]. Phase composition was measured by x-ray diffraction (XRD) (Rigaku SmartLab diffractometer, Tokyo, Japan) over the range of 5–90 $2\theta$ degrees, with a step size of 0.02 degrees and a dwell time of 0.5 s per step. The only impurity was found to be TiC (3.6%).

Prior to the impact tests, the longitudinal, $c_l = 9.22 \pm 0.01$ km/s, shear, $c_s = 5.69 \pm 0.02$ km/s, and bulk $[c_b = \sqrt{c_l^2 - (4/3)c_s^2} = 6.47 \pm 0.02\ km/s]$ speeds of sound were determined using an ultrasonic pulse-echo technique. The initial sample density, $\rho_0$, measured by the Archimedes method was $4.54 \pm 0.01\ Mg/m^3$. All these values are on par with previously reported ones by Radovic *et al.* [37].

Since no information on the behavior of $Ti_3SiC_2$ under planar impact loading was available, the first set of experiments were carried out with polymethylmethacrylate (PMMA) window. Here the 3-mm-thick samples were backed with a 6-mm-thick PMMA window preventing premature damage of the rear (unimpacted) sample surface upon the shock wave's arrival. In this first series of experiments, the samples—initially at ambient temperatures ~300 K—were loaded by 0.5 mm Cu or 1 mm W impactors accelerated using a 25 mm smooth bore gun to velocities that ranged from 200 to 1040 m/s. The velocity of the sample/window interface was continuously monitored by VISAR having interferometric constants of 96.4 and 439.2 m/s per fringe. One of the outcomes of this first series of experiments was understanding that until the impact velocity exceeded the 1 km/s level, the experiments could be performed with samples whose rear surfaces were free (windowless). This essentially simplified the next series of tests.

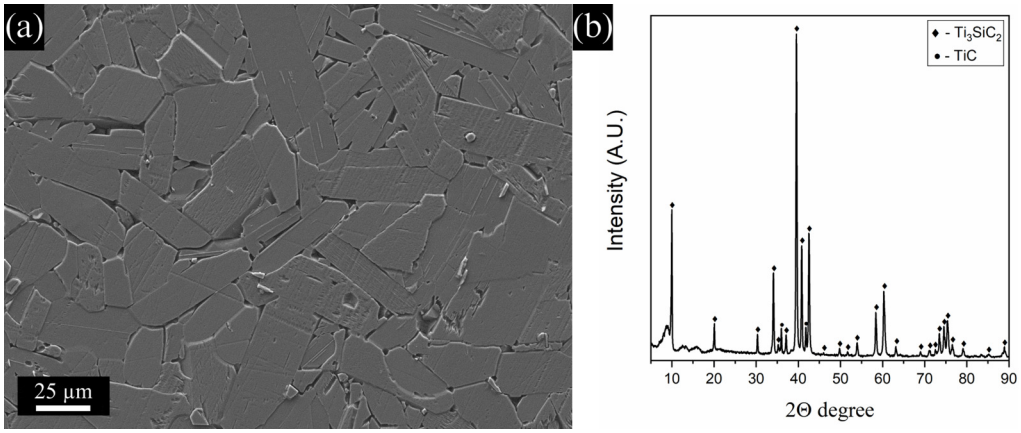


FIG. 2. (a) Typical SEM microstructure of a polished and etched $Ti_3SiC_2$ sample studied herein. (b) XRD pattern of the $Ti_3SiC_2$ sample.

The velocity monitored by VISAR in series II–IV (see below) is thus the velocity of the free sample surface. In these tests, the VISAR interferometric constant was 96.4 m/s/fringe. In all experiments, the impact velocity (with an uncertainty of about 0.5%) was controlled by two pairs of electrical charged pins and by two in-barrel fiber optic stations.

The second series of tests was also performed on 3-mm-thick samples whose temperature was varied between 300 and 1200 K. These samples underwent relatively modest loading by the 1 mm Cu impactors with a velocity of 210 ± 10 m/s. In the third and fourth series of experiments, 0.5-, 1-, and 2-mm-thick samples were exposed to the same loading conditions in the 300–900 K temperature range. The details of how the samples were preheated with a resistive heater up to temperatures of about 1400 K, with ∼10 K uncertainty, can be found elsewhere [38]. For the ambient temperature tests, the same assembly, this time without a heater, thermal screen, or thermocouple, was used.

## III. RESULTS AND ANALYSIS

### A. Principal Hugoniot of $Ti_3SiC_2$

Because materials have different compressibility in the elastic and inelastic (plastic) states, the front of the rectangular stress pulse generated at the sample surface by the planar impact is unstable and splits into (i) an elastic precursor wave with an amplitude corresponding to the material's Hugoniot elastic limit (HEL) propagating through the sample with a velocity close to the longitudinal speed of sound, $c_l$, and (ii) a plastic wave whose propagation velocity is close to the bulk speed of sound, $c_b$ ($c_b < c_l$). This two-wave structure is apparent in the velocity histories $u(t)$, recorded at the interfaces between differently loaded samples and the PMMA windows shown in Fig. 3(a). Using PMMA shock Hugoniot data [39] and a shock correction for the index of refraction of the PMMA window [39,40], the stress at HEL, $\sigma_{\mathrm{HEL}}$, can be estimated from Eq. (1) [41]:

$$\sigma_{\mathrm{HEL}} = \tfrac{1}{2}\left(\rho_0^{\mathrm{Ti_3SiC_2}} c_l^{\mathrm{Ti_3SiC_2}} + \rho_0^{\mathrm{PMMA}} c_l^{\mathrm{PMMA}}\right) u_{\mathrm{HEL}} = 0.18\ \mathrm{GPa}. \tag{1}$$

This value corresponds to a shear stress at HEL, $\tau_{\mathrm{HEL}} = (c_s^2/c_l^2)\sigma_{\mathrm{HEL}} = 70$ MPa, and to a yield strength $Y \approx 2\tau_{\mathrm{HEL}} =$ 140 MPa [42], which is four to six times lower than values measured in quasistatic compression tests [43–46].

Taking into account the physical properties of PMMA [39,40] and applying, in sequence, the mass and momentum conservation laws to the elastic and plastic waves [47], one obtains the shock wave propagation velocity ($U_s$), compressive stress ($\sigma_H$), specific volume ($V_H$), and compressive strain (positive) $\eta_H = 1 - V_H/V_0$ at the final, Hugoniot state. Figure 3(b) plots the dependence of $U_s$ and $\sigma_H$ on particle velocity, $u_p = \sqrt{\sigma_H \eta_H/\rho_0}$. As is apparent from Fig. 3(b), the $U_s$ values obtained after the two high-energy impact tests, together with $c_b$, may be approximated—with reasonable accuracy with a Pearson correlation coefficient >0.999—by the linear expression $U_s = C_0 + su_p = 6.47 + 1.61u_p$, where $s$ is the slope and $C_0$ is the intercept. This means that $C_0$ of the linear Hugoniot virtually coincides with $c_b$, and that for $u_p > 650-700$ m/s, the sample behind the shock front is close to being in a state of pure *hydrostatic compression*. Accordingly, the expression for the Hugoniot hydrostat is $p_H = \rho_0(C_0 + su_p)u_p = 29.37u_p + 7.32u_p^2$.

### B. Temperature dependence of dynamic yield and tensile (spall) strengths of $Ti_3SiC_2$

As noted above, only the first series of samples were backed with a PMMA window. The velocities measured in all other series were those of free sample surfaces. Figure 4(a) displays the free surface velocity histories for 3-mm-thick samples preheated to temperatures ($T_0$) of 300, 600, 900, and 1200 K and shock-loaded with a 1 mm Cu impactor with a velocity of ≈210 m/s. As is apparent from Fig. 4(a), varying $T_0$ does not change the waveforms substantially. The main changes occur during the initial stages of shock compression. The inset in Fig. 4(a) shows that the part of the waveforms associated with the elastic-plastic transition varied systematically with $T_0$. As in the case of the waveforms [Fig. 4(a)] in the previous subsection, the elastic deformation associated with a velocity ramp may be caused by either some dispersion of the wave due to the presence of multiple grain boundaries and/or ripplocations, or by the relatively low stresses needed to split low-energy core dislocations [48]. Note that the distinct signature of an elastic-to-plastic transition is absent in the waveforms of Fig. 4(a). This results in substantial uncertainty

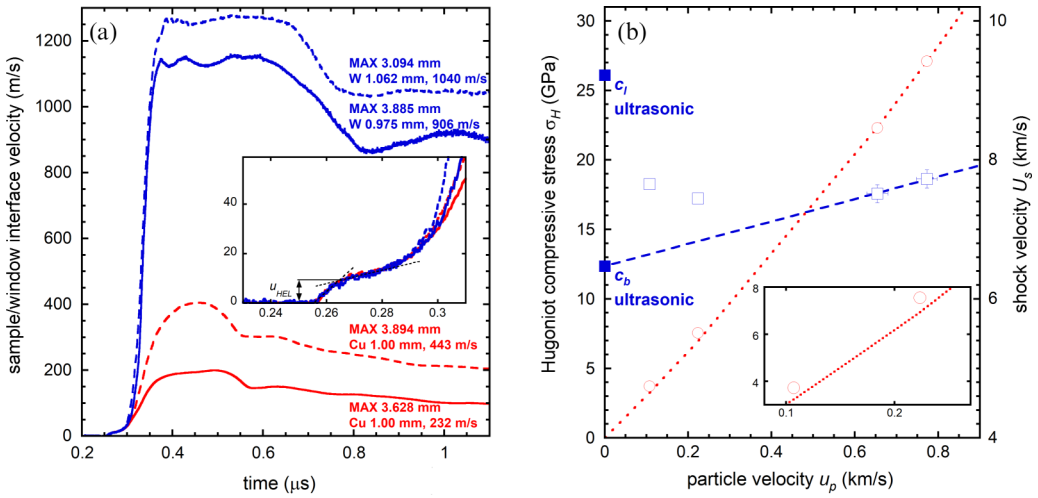


FIG. 3. (a) Velocity histories of $Ti_3SiC_2$/PMMA interfaces recorded after impacts of different strengths. Sample and impactor thicknesses and impactor velocities are listed next to the waveforms. The inset shows a determination of $u_{HEL}$ used for estimating $\sigma_{HEL}$. (b) Shock velocities $U_s$ (open squares, right-hand $y$ axis) and stress $\sigma_H$ (open circles, left-hand $y$ axis) at Hugoniot determined from the velocity histories shown in (a) as a function of particle velocity $u_p$. Filled squares correspond to the ultrasonic speed of sound in $Ti_3SiC_2$. The dashed line is a linear approximation. The dotted line is the Hugoniot hydrostat $p_H = \rho_0 U_s u_p$. Inset shows a departure of $\sigma_H$ values from the hydrostat. Error bars correspond to the uncertainty in determinations of $U_s$ and $u_p$.

in the determination of $u_{HEL}$ by the method shown in the inset of Fig. 4(a). This uncertainly is propagated to estimates of $\sigma_{HEL}$ and yield strength, $Y$, given by [42]

$$\sigma_{HEL} = \frac{1}{2}\rho_0 c_l u_{HEL}, \tag{2a}$$

$$Y = 2\frac{c_s^2}{c_l^2}\sigma_{HEL}. \tag{2b}$$

To make use of Eqs. (2a) and (2b), $c_l$ and $c_s$ (or of moduli $E' = \rho_0 c_l^2$) and of the densities $\rho_0$ at $T_0$ need to be known [37,49]. It will be shown later that the two-wave (i.e., an elastic precursor wave followed by a plastic wave) configuration obtained with the 3-mm-thick samples may be considered as steady. In such a case, the simple wave approximation [50,51] may be applied to the waveforms of Fig. 4(a) to obtain, based on the experimentally measured velocity histories, the compressive stress-strain function $\sigma(\varepsilon)$ of $Ti_3SiC_2$, as described in parametric form in the Appendix.

At the impactor/sample interface, the planar impact generates a compressive stress pulse traveling toward the free surfaces of both the impactor and sample free surfaces. After reflection from the surfaces, both compressive waves start to travel back toward the impactor/sample interface, now as

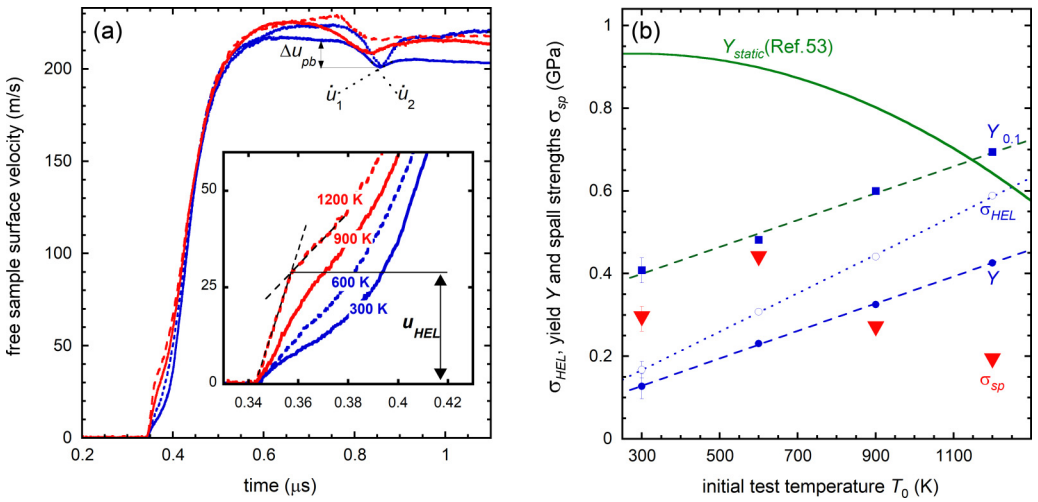


FIG. 4. (a) Free sample surface velocity histories of 3-mm-thick $Ti_3SiC_2$ samples, preheated to different temperatures, $T_0$ (labeled by the waveforms in inset). Inset zooms on short times. Arrows and dotted lines show the waveforms' parameters used for determining the yield and spall strengths. (b) Stress at $\sigma_{HEL}$(open circles), yield $Y$ (filled circles), offset yield $Y_{0.1}$ (filled squares), and spall strength $\sigma_{sp}$ (filled red triangles) as a function of $T_0$. Dashed and dotted lines are the linear fits of $Y$, $Y_{0.1}$, and $\sigma_{HEL}$, respectively. Solid line reproduces results of Ref. [53] obtained under compression using a strain rate of $\approx 10^{-4}\,s^{-1}$. Error bars correspond to the typical uncertainty of the property measured.

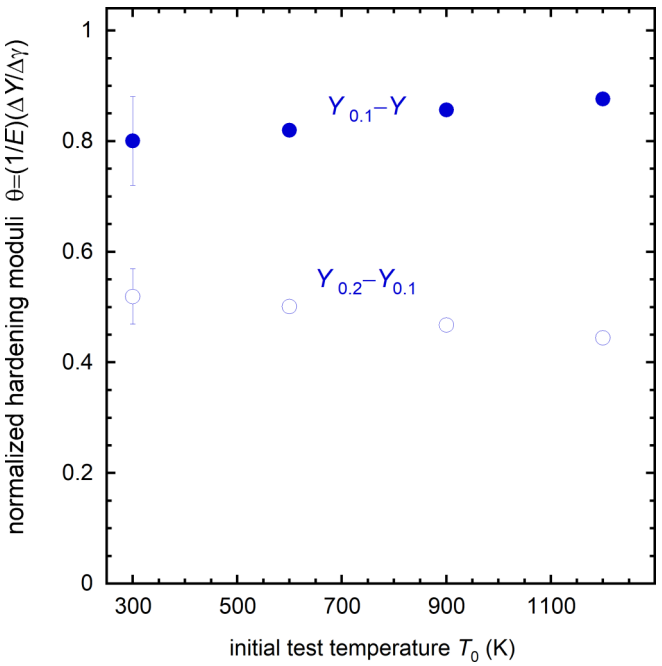


FIG. 5. Normalized strain hardening moduli $\theta$ determined based on $Y_{0.1} - Y$ (filled circles) and $Y_{0.2} - Y_{0.1}$ (open circles) increments as a function of $T_0$. Error bars correspond to the relatively high, ≈10%, uncertainty in the determination of $\theta$.

release (or rarefaction) waves. The arrival of the rarefaction wave from the impactor rear surface to the rear surface of the sample starts to decrease its velocity from the maximum $u_H$ value. The deceleration is, however, limited by the material strength, which is virtually proportional to the velocity pull-back $\Delta u_{\rm pb}$ [Fig. 4(a)]. The in-sample collision of two rarefaction waves results in the generation of a tensile stress pulse at the site of the collision. If the so-generated tensile stress exceeds the tensile strength of the sample, dynamic tensile (spall) fracture takes place. The fracture is accompanied by the creation of two new surfaces at the collision site and by the generation of a compressive signal that changes deceleration of the sample's rear surface into acceleration followed by velocity minima shown in Fig. 4(a).

The dynamic tensile or spall strength $\sigma_{\rm sp}$ can thus be estimated assuming [52]

$$\sigma_{\rm sp} = \tfrac{1}{2}\rho_0 c_b(\Delta u_{\rm pb} + \delta u), \tag{3}$$

where $\delta u = d_{\rm sp}(1/c_b - 1/c_l)|\dot{u}_1|\dot{u}_2/(|\dot{u}_1| + \dot{u}_2)$ is a correction for the distortion of the waveform as a result of the different propagation velocities of the spall signal front and of the rarefaction wave ahead of it in the elastic-plastic medium [52], and $d_{\rm sp}$ is the thickness of the spall plate, which is virtually equal to the impactor thickness. The temperature dependencies of $\sigma_{\rm HEL}$, $Y$, $Y_{0.1}$, and $\sigma_{\rm sp}$, determined based on Eqs. (2)–(4), are plotted in Fig. 4(b) together with the quasistatic (strain rate $10^{-4}$ s$^{-1}$) compressive strength results taken from Ref. [53]. What is quite intriguing and worth mentioning is the maximum in $\sigma_{\rm sp}$ observed at 600 K, which is discussed below in Sec. IV B.

Figure 5 displays the work hardening moduli ($\theta$), normalized by Young's modulus ($E$), viz. $\theta = (1/E)(\Delta Y/\Delta\gamma)$, employing two yield strength increments $Y_{0.1} - Y$ and $Y_{0.2} - Y_{0.1}$. Considering the uncertainties in the determination of the values of $\theta$ for the former and the latter intervals, these values can be considered, as shown in Fig. 5, to be temperature-independent and equal to ≈0.8 and ≈0.5, respectively.

### C. Relaxation of shear stress in shock-loaded $Ti_3SiC_2$

To better understand the processes governing plastic deformation, we carried out two additional series of impact tests on samples of different thicknesses shock-loaded at 300 and 900 K. As noted above, the shock front in the elastic-plastic material is unstable and splits into elastic and plastic waves traveling with different velocities. Initially, at the impacted surface, the shear stresses are relatively high. In particular, in the case of the tests whose results are shown in Fig. 4(a), it is about $\tau_{\rm in} \approx (c_s^2/c_l^2)(\rho_0 c_l u_H/2)$ or, normalized by the shear modulus $G = \rho_0 c_s^2$, $\tau_{\rm in}/G \approx u_H/2c_l \approx 6 \times 10^{-3}$. After the 3 mm traverse [for, e.g., a 300 K test, Fig. 4(a)], $\tau_{\rm HEL}/G \approx 9 \times 10^{-4}$ is significantly reduced, i.e., the elastic precursor wave decays with propagation distance and the shear stress behind the precursor front relaxes. Evidently, the relaxation occurs at the expense of plastic deformation.

Duvall *et al.* [54] showed that in an acoustic approximation, the variation of $\sigma_{\rm HEL}$ (and $\tau_{\rm HEL}$ as well) with propagation distance ($h$) is related to the initial plastic strain rate $\dot{\gamma}$ as

$$\frac{d\sigma_{\rm HEL}}{dh} = -\frac{4}{3}\frac{G\dot{\gamma}}{c_l}. \tag{4}$$

The two-test series with samples of various thicknesses were performed with the goal of obtaining the dependences $\sigma_{\rm HEL}(h)$ at different $T_0$. The sample free surface velocity histories recorded in these series are presented in Figs. 6(a) and 6(b) for $T_0$ of 300 and 900 K, respectively. Note that the time along the $x$ axis is normalized as $t^* = tc_l/d$, where $t$ is the time and $d$ is the sample thickness. This is done to account for the additional time that it takes for the shock wave to travel in samples of different thicknesses [42].

To quantify the amplitude decay of the elastic wave with $h$ [Eq. (4)], we used both $\sigma_{\rm HEL}$ [as defined in Eqs. (2a) and (2b)] and $\sigma_{\rm HEL0.1}$ [equal to the compressive stress corresponding to a plastic strain $\gamma = 0.001$; see Eqs. (A1) and (A5)]. The latter, however, requires a reservation. Equations (A1)–(A5) are applicable when the flow is steady [50], i.e., when all the waveforms shown in Fig. 6(a) or 6(b) coincide. Using Eqs. (A2) and (A6) in the case of a relaxing solid is limited to very low levels of plastic strain, when the uncertainties in the stress and plastic strain are not too large. It may be some 2–3 % in the case of the 2 or 3 mm samples, but it may approach 10% for the 0.5 mm samples.

The values of $\sigma_{\rm HEL}$ and $\sigma_{\rm HEL0.1}$ estimated at 300 and 900 K are shown in Fig. 7 as a function of $h$ for different $d$. As is apparent from Fig. 7, with reasonable accuracy (a Pearson correlation coefficient better than 0.99), all the dependencies may be fit by a power function

$$\sigma(h) = \sigma_0(h/h_0)^{-\alpha}, \tag{5}$$

where $h_0 = 1$ mm, and $\sigma_0$ and $\alpha$ are fitting parameters whose values for both $\sigma_{\rm HEL}$ and $\sigma_{\rm HEL0.1}$ are listed in Table I as a function of $T_0$.

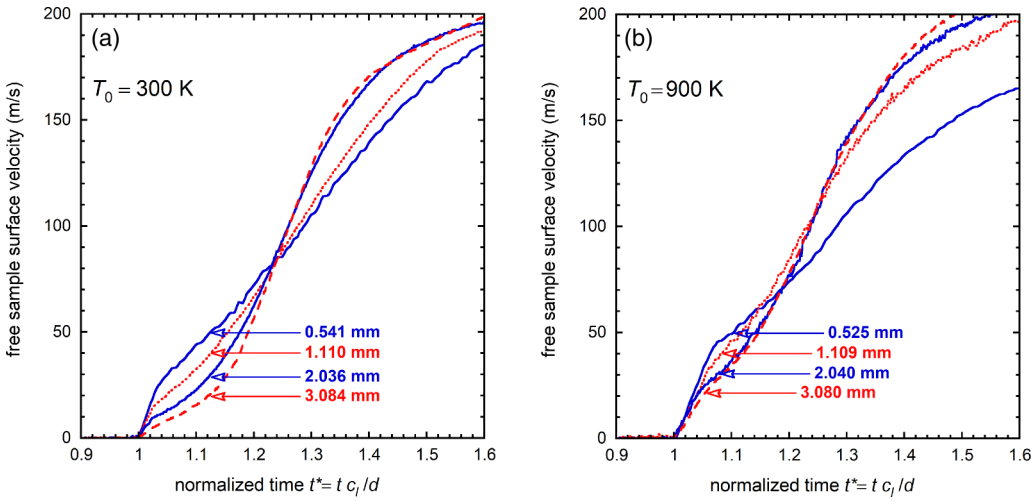


FIG. 6. Free surface velocity histories for samples of different thicknesses (indicated to the right of waveforms) shock loaded at $T_0$ of (a) 300 K and (b) 900 K.

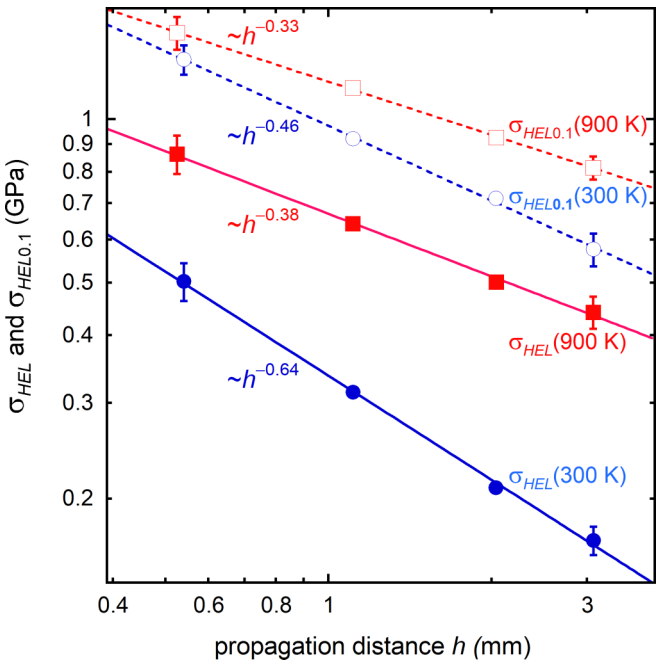


FIG. 7. Log-log plot of $\sigma_{\mathrm{HEL}}$(filled symbols) and $\sigma_{\mathrm{HEL0.1}}$(open symbols) as a function of propagation distance at 300 and 900 K. Solid and dashed lines are the power fits $\sigma(h) = \sigma_0(h/h_0)^{-\alpha}$. Error bars correspond to typical uncertainties in stress measurements for the 0.5- and 3-mm-thick samples.

TABLE I. Parameters of elastic precursor decay in $Ti_3SiC_2$ at different temperatures. Values in parentheses correspond to uncertainty of the last digit of the calculated parameter.

| $T_0$(K) | Stress | $\sigma_0$(GPa) | $\alpha$ | $m$ | $A$(GPa s$^m$) | $\dot{\gamma}$(1 mm)(s$^{-1}$) |
|---|---|---|---|---|---|---|
| 300 | $\sigma_{\mathrm{HEL}}$ | 0.34(1) | 0.64(2) | 0.39 | $9.28 \times 10^6$ | $1.01 \times 10^4$ |
| 300 | $\sigma_{\mathrm{HEL0.1}}$ | 0.97(5) | 0.46(3) | 0.32 | $4.01 \times 10^7$ | $2.11 \times 10^4$ |
| 900 | $\sigma_{\mathrm{HEL}}$ | 0.67(2) | 0.38(2) | 0.28 | $4.73 \times 10^7$ | $1.29 \times 10^4$ |
| 900 | $\sigma_{\mathrm{HEL0.1}}$ | 1.8(1) | 0.33(3) | 0.25 | $1.37 \times 10^8$ | $2.98 \times 10^4$ |

Combining (4) and (5), it is possible to relate $\sigma_{\mathrm{HEL}}$ with the initial plastic strain rate:

$$\sigma_{\mathrm{HEL}} = \sigma_0 \left( \frac{4}{3\alpha} \frac{h_0}{c_l} \frac{G}{\sigma_0} \dot{\gamma} \right)^{\frac{\alpha}{\alpha+1}} = A \dot{\gamma}^m, \tag{6}$$

where $A$ is the strain rate factor with units GPa s$^m$, and $m$ is the strain-rate exponent. The values of $m$, $A$, and, for reference, the strain rate after a 1 mm traverse, are listed, respectively, in the three rightmost columns of Table I.

Had the deformation been dislocation-based (not in our case), then the decay parameters shown in Table I could be used to shed more light on the problem. As mentioned above, all determined $\alpha$ values are typical for the control of dislocation motion and multiplication by phonon viscous drag. In such a case, the average dislocation velocity $\bar{v}$ is related to the applied shear stress $\tau$ via the linear expression [55]

$$\bar{v} = \frac{b}{B} \tau, \tag{7}$$

where $b$ is the dislocation Burgers vector, and $B$ is the phonon drag coefficient, responsible for the increase in both $\sigma_{\mathrm{HEL}}$ and $\sigma_{\mathrm{HEL0.1}}$ with increasing temperatures in metals. Substituting Eq. (7) into Orowan's equation, one obtains

$$\dot{\gamma} = \rho_m b \bar{v} = \rho_m \frac{b^2}{B} \tau, \tag{8}$$

where $\rho_m$ is the density of mobile dislocations. Since information on $B$ in $Ti_3SiC_2$ is unavailable, estimating $\rho_m$ from Eq. (8) is impossible. It is possible, however, to estimate the ratio $\rho_{\mathrm{mf}}/\rho_{\mathrm{mi}}$ between the density corresponding to the very beginning of plastic deformation, $\rho_{\mathrm{mi}}$, and the density $\rho_{\mathrm{mf}}$ after some finite plastic deformation, e.g., $\gamma = 0.001$. Combining Eqs. (4), (5), and (8) for the same $h$, one obtains

$$\frac{\rho_{\mathrm{mf}}}{\rho_{\mathrm{mi}}} = \frac{\dot{\gamma}_f \sigma_{\mathrm{HEL}i}}{\dot{\gamma}_i \sigma_{\mathrm{HEL}f}} = \frac{\alpha_f}{\alpha_i}. \tag{9}$$

Substituting the values of $\alpha$ from Table I into Eq. (9) leads to the conclusion that increasing the strain from virtually 0 to 0.001 *decreases* $\rho_m$ by 30% at 300 K and by 10% and

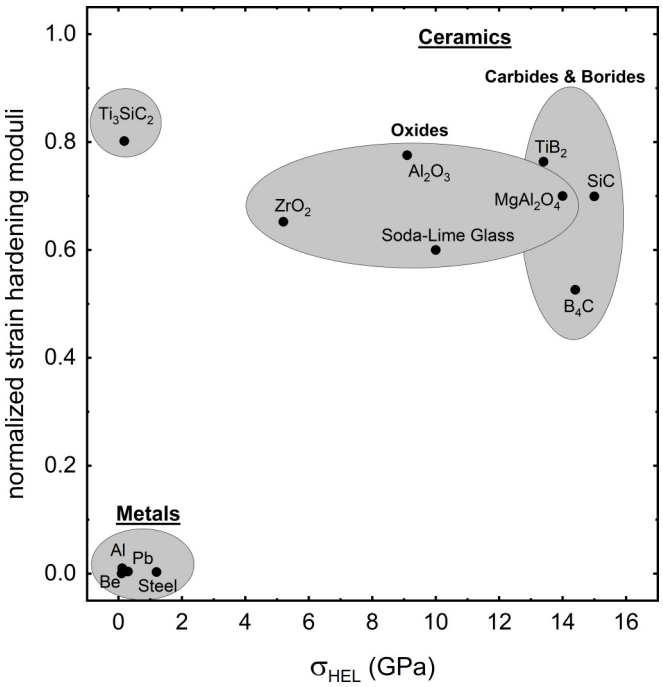


FIG. 8. Normalized strain hardening moduli as a function of HEL for various materials [56–62].

900 K. Given the very high hardening rates observed, such a conclusion is physically untenable (see below).

## IV. DISCUSSION

The most important result of this work is the uniqueness of the response of $Ti_3SiC_2$ *vis-à-vis* what is known to date about how metals and ceramics respond to high strain rates. This is best seen in Fig. 8, where the normalized strain hardening moduli are plotted as a function of $\sigma_{HEL}$ for various metals and ceramics. From this plot alone, it is clear that $Ti_3SiC_2$, and presumably other MAX phases, is an outlier. The leitmotiv of what follows is that in some respects $Ti_3SiC_2$ behaves like a ductile metal but, crucially, in others it behaves more like a hard, brittle ceramic material. In other words, $Ti_3SiC_2$ behaves like nothing before it and thus this response probably reflects how ripplocations respond to very high strain rates. We note in passing that in the case of the carbides and borides shown in Fig. 8, the post HEL behavior is brittle, and immediately after HEL the material is damaged. Moreover, the post-HEL ramping of the signal (for example, particle velocity) is terminated in the compressive front whose velocity is essentially lower than the bulk speed of sound of pristine material.

### A. Principal Hugoniot of $Ti_3SiC_2$

The first surprise is the fact that all the waveforms of the velocity histories [Fig. 3(a)] are *atypical for ceramic materials and are more reminiscent of metals*. The elastic precursor wave—with a very modest amplitude ($u_{HEL} \approx 8$ m/s versus hundreds of m/s typical for ceramics)—is followed by a plastic wave terminated at the Hugoniot.

From Fig. 3(b) it is clear that $\sigma_H$ of the lower velocity tests (232 and 443 m/s) lie some 0.5 GPa apart from the hydrostat. This, in turn, suggests that the Hugoniot state, achieved by relatively low-energy impacts, corresponds to a shear stress of about $\tau = 3(\sigma_H - p_H)/4 \approx 380$ MPa. By comparing this value, corresponding to the final stage of shock-induced plastic deformation, with that at its very beginning (HEL), it is reasonable to conclude that plastic deformation of $Ti_3SiC_2$, under relatively low impact energies, is accompanied by *quite strong work hardening more typical of ceramics than metals* (Fig. 8). As discussed in the Introduction, we have recently shown that such high hardening rates and moduli are a hallmark of deformation by ripplocations [16].

Lastly in this section, it is important to note that under more intense loading conditions the complete comminution of the sample occurs accompanied by the vanishing of the deviatoric stresses and a loss of shear strength. This statement is justified by estimating the spall strength of $Ti_3SiC_2$ based on the velocity histories in Fig. 3(a). While measuring the spall strength in experiments with low-impedance windows, as is done herein, is accompanied by substantial uncertainties [41], the spall strength for the 232 and 443 m/s impacts is small but finite, viz. $0.29 \pm 0.05$ and $0.32 \pm 0.06$ GPa, respectively. The spall strength determined for stronger impacts is thus definitely zero, which is *typical of ceramics* shock-compressed above their HEL.

### B. Temperature dependence of dynamic yield and tensile (spall) strengths of $Ti_3SiC_2$

The temperature dependencies shown in Fig. 4(b) are striking in that the ambient values of $Y$ and $Y_{0.1}$ are low and increase with increasing temperatures. Such a response is atypical for ceramics and *more typical of pure metals,* with relatively low Peierls stresses. In contradistinction, under static loading conditions [Fig. 4(b)] the strengths decrease with increasing temperatures, which suggests thermal activation.

To date, two mechanisms have been proposed to explain the increases in $Y$ and $Y_{0.1}$ with temperature [Fig. 2(b)]: (i) an increased stacking fault energy with temperature, resulting in a decrease in dislocations mobility; and/or (ii) viscous phonon drag of dislocations that increases with increasing temperatures [55]. The latter mechanism controls dislocation motion when the acting shear stress is higher than the Peierls stress and dislocation glide is the overbarrier type [63]. Since neither applies to $Ti_3SiC_2$, they cannot be invoked here.

As is apparent from Fig. 4(b), and although the temperature dependences of $Y$ and $Y_{0.1}$ are parallel, the absolute values of $Y_{0.1}$ are significantly higher. It was noted in Sec. IV A that the RT impact response is associated with substantial work hardening, quantified in Fig. 5. Usually the values of the strain hardening moduli in strongly work hardened fcc metals are about $10^{-3}$–$10^{-2}$ [61,64,65], i.e., the strain hardening moduli of $Ti_3SiC_2$ (0.3–0.6, Table I) are extraordinarily high, even by metallic standards.

The temperature dependence of the spall strength $\sigma_{sp}$ shown in Fig. 4(b) points to one more aspect of the *dual nature* of $Ti_3SiC_2$. Although the spall strength is more than modest, the values of $\sigma_{sp}$ over the 300–600 K temperature interval are twice as high as its $\sigma_{HEL}$. Such a ratio between the dynamic tensile and compressive strengths is again typical of *metals*. Moreover, taking into account that the spall process comprises

nucleation of voids and their growth followed by voids coalescence [52], and remarking that over this temperature interval (up to 600 K) $\sigma_{sp}$ and $Y$ correlate, one can conclude that over this temperature interval the spall process is governed by the growth of voids. However, it is not the case at temperatures higher than 600 K, where the behavior changes to that more common of ceramics. In ceramics, the $\sigma_{sp}$ values are typically smaller than $\sigma_{HEL}$ and no $\sigma_{sp}$-$Y$ correlations are observed. It follows that at higher temperatures, control of the spall process seems to be passed to void or microcrack nucleation. It is worth mentioning that information about the temperature variation of the spall strength of any material (not only the MAX phases) is extremely scarce in the literature.

### C. Relaxation of shear stress in shock-loaded $Ti_3SiC_2$

At first glance, three things are apparent from Fig. 6: (i) in both cases, the amplitudes of the elastic precursor waves decrease with propagation distance, (ii) the amplitudes of the elastic waves are greater at 900 K than those obtained at ambient temperatures, and (iii) the time intervals between the elastic and plastic waves are smaller at higher temperatures. The latter is possibly related to a faster decline with temperature of the longitudinal modulus $E' = \rho_0 c_l^2$ versus the bulk modulus $B = \rho_0 c_b^2$ [66].

Regardless of whether $\sigma_{HEL}$ or $\sigma_{HEL0.1}$ is considered, their decrease with $h$ (Fig. 7) is *reminiscent* of *metals with relatively low Peierls stresses* [63]. The fitted exponent $\alpha$ is in the 0.3–0.7 range (Table I), which is typical for overbarrier glide of dislocations and also shows some decline with temperature as occurs in pure Al [67] or Cu [68]. However, substituting these $\alpha$ values into Eq. (10) leads to the physically untenable result that increasing the strain from virtually 0 to 0.001, the density of mobile dislocations—if invoked—should *decrease* by some 30% at 300 K and by 10% and 900 K. Since such a conclusion is at odds with the large hardening rates observed herein, it is reasonable to conclude that the deformation is *not* mediated by basal dislocations.

Returning to Fig. 8, it is obvious that $Ti_3SiC_2$ is an outlier, with $\theta$ values more typical of ceramics, but $\sigma_{HEL}$ values that are reminiscent of metals. Based on these crucial results, we reach the following tentative conclusion: The signature of layered solids that deform by ripplocations is one where $\sigma_{HEL}$ is quite low and comparable to that of metals, while simultaneously having normalized hardening rates comparable to typical ceramics.

Currently, there is an existing body of work that is rapidly expanding that suggests that deformation in layered solids is not mediated by BDs, but rather by ripplocations [14,16–21]. The results of this work comprise one more set of results that cannot be explained by dislocations in general, or more specifically, BDs (the only kind assumed present in layered solids). The very high hardening rates observed herein have been observed previously in nanoindentation experiments of $Ti_3SiC_2$ [16]. Since in this case no external confinement was applied, as in a nanoindentation experiment, the bulk of the sample itself acts as its own confinement. We have also previously argued that the dependence of the failure stresses on confinement can be taken as a good indication that ripplocations, and not BDs, are the operative micromechanism [16,18]. Nothing in this work contradicts any of these conclusions; if anything, it confirms them.

Lastly, we have recently shown using transmission electron microscopy that at the atomic level deformed biotite was riddled by ripplocation bridges that in some cases were a few atomic layers thick, and in other cases were much thicker [20]. These bridges could not have formed as a result of BD motion.

## V. SUMMARY AND CONCLUSIONS

Herein the dynamic properties, at strain rates of $>10^4\ s^{-1}$, such as Hugoniot hydrostat, Hugoniot elastic limit, yield strength, spallation strength, and normalized work hardening moduli of the MAX phase $Ti_3SiC_2$, were determined. Additionally, the temperature dependencies of dynamic yield and tensile spallation strengths were established.

It was found that the elastic precursor wave has a relatively low amplitude that was followed by a plastic wave, terminated at the Hugoniot. Such behavior is typical of ductile metals. However, during plastic deformation, the work hardening rates were quite high and more typical of ceramics subjected to dynamic loading.

The yield strengths were also found to increase linearly with increasing test temperatures, which is atypical for ceramics. The temperature dependency of the spallation strength, however, was found to be quite similar to the quasistatic yield strength dependency. However, the values of $\sigma_{sp}$ were found to be double the $\sigma_{HEL}$ values, which again is more typical of metals.

Lastly, we show that if standard dislocation-based theory is used to estimate the mobile dislocation density, $\rho_m$, we reach the untenable conclusion that $\rho_m$ decreases by 30% as the plastic strain rate increases from 0 to 0.001%. Our results, however, are at least qualitatively consistent with the presence of ripplocations and ripplocation boundaries.

This conclusion is of paramount importance because at this time, a totally new fracture mechanics at high strain rates—and slow ones for that matter—of layered solids has to be developed. As shown herein, dislocation theory is of little use. This work could also be of great importance to seismology and seismologists at both the geological and nanoscales.

## ACKNOWLEDGMENTS

This work was funded by the CMMI division of the National Science Foundation under Grant No. 1728041. The authors also acknowledge financial support from the Israeli Science Foundation (Grant No. 441/18) and the Israeli Ministry of Defense (Grant No. 87576431) (E.Z.). The authors thank Dr. Sankalp Kota of Drexel University for valuable discussions.

## APPENDIX: COMPRESSIVE STRESS-STRAIN FUNCTION $\sigma(\varepsilon)$

Assuming that the compressive part of the velocity history $[u(t)]$ is a result of propagation of a simple wave, having Lagrangian velocity $[a(u)]$ through the sample, the mass-

momentum conservation equations are as follows:

$$V = -\frac{1}{2}\int_0^{u_H} \frac{du}{\rho_0 a(u)}, \tag{A1}$$

$$\sigma = \frac{1}{2}\rho_0 \int_0^{u_H} a(u)du, \tag{A2}$$

where $\sigma$ is considered as positive in compression, the factor ½ reflects the assumption that the particle velocity ($u_p$) is equal to one-half of the free surface velocity ($u$), and $u_H$ is the particle velocity at the top (on Hugoniot) of the shock wave. The specific volume $V$ is related to the engineering strain by $\varepsilon = (V_0 - V)/V_0$, where $V_0$ is the initial specific volume.

The $a(u)$ of propagation of the signal—with time $t(u)$—corresponding to the particle velocity value $u_p = u/2$ through a sample of thickness $d$ is

$$a = c_l \frac{d/c_l - \Delta t(u)/2}{d/c_l + \Delta t(u)/2}, \tag{A3}$$

where $\Delta t(u) = t(u) - t(u = 0) = t(u) - d/c_l$.

Knowledge of the material Hugoniot hydrostat, $U_s = C_0 + su_p$, gives the pressure

$$p(\varepsilon) = \rho_0 C_0^2 \frac{\varepsilon}{(1 - s\varepsilon)^2} \tag{A4}$$

at the temperature of interest and allows us to find the dependencies of shear, $\tau$,

$$\tau = \tfrac{3}{4}[\sigma(\varepsilon) - p(\varepsilon)], \tag{A5}$$

and yield, $Y = 2\tau$, stresses on the plastic strain,

$$\gamma = \int_0^u \left(\frac{du}{a} - \frac{d\tau}{G}\right). \tag{A6}$$

When the dependence $Y(\gamma)$ is obtained, the 0.1% proof stress $Y_{0.1} = Y(\gamma = 0.001)$ can be found. The $Ti_3SiC_2$ Hugoniot hydrostat $U_s = C_0 + su_p = 6.47 + 1.61u_p$ is known only at 300 K. Here we assume that this hydrostat and $c_b$ are not functions of temperature.


[1] M. W. Barsoum, The $M_{N+1}AX_N$ phases: A new class of solids: Thermodynamically stable nanolaminates, Prog. Solid State Chem. **28**, 201 (2000).

[2] M. Sokol, V. Natu, S. Kota, and M. W. Barsoum, On the chemical diversity of the MAX phases, Trends Chem. **1**, 210 (2019).

[3] X. H. Wang and Y. C. Zhou, Layered machinable and electrically conductive $Ti_2AlC$ and $Ti_3AlC_2$ ceramics: A review, J. Mater. Sci. Technol. **26**, 385 (2010).

[4] Z. M. Sun, Progress in research and development on MAX phases: a family of layered ternary compounds, Int. Mater. Rev. **56**, 143 (2011).

[5] M. Barsoum and T. El-Raghy, The MAX phases: Unique new carbide and nitride materials, Am. Sci. **89**, 334 (2001).

[6] M. W. Barsoum and M. Radovic, Elastic and Mechanical Properties of the MAX Phases, Annu. Rev. Mater. Res. **41**, 195 (2011).

[7] B. T. Kelly, *Physics of Graphite*, Applied Science (1981).

[8] R. Christoffersen and A. K. Kronenberg, Dislocation interactions in experimentally deformed biotite, J. Struct. Geol. **15**, 1077 (1993).

[9] F. C. Frank and A. N. Stroh, On the theory of kinking, Proc. Phys. Soc. Sect. B **65**, 811 (1952).

[10] M. W. Barsoum, T. Zhen, A. Zhou, S. Basu, and S. R. Kalidindi, Microscale modeling of kinking nonlinear elastic solids, Phys. Rev. B **71**, 134101 (2005).

[11] M. A. Biot, Further development of the theory of internal buckling of multilayers, GSA Bull. **76**, 833 (1965).

[12] P. J. Hudleston and S. H. Treagus, Information from folds: A review, J. Struct. Geol. **32**, 2042 (2010).

[13] S. R. Reid and C. Peng, Dynamic uniaxial crushing of wood, Int. J. Impact Eng. **19**, 531 (1997).

[14] M. W. Barsoum, X. Zhao, S. Shanazarov, A. Romanchuk, S. Koumlis, S. J. Pagano, L. Lamberson, and G. J. Tucker, Ripplocations: A universal deformation mechanism in layered solids, Phys. Rev. Mater. **3**, 013602 (2019).

[15] A. Kushima, X. Qian, P. Zhao, S. Zhang, and J. Li, Ripplocations in van der Waals Layers, Nano Lett. **15**, 1302 (2015).

[16] J. Griggs, A. C. Lang, J. Gruber, G. J. Tucker, M. L. Taheri, and M. W. Barsoum, Spherical nanoindentation, modeling and transmission electron microscopy evidence for ripplocations in $Ti_3SiC_2$, Acta Mater. **131**, 141 (2017).

[17] J. Gruber, A. C. Lang, J. Griggs, M. L. Taheri, G. J. Tucker, and M. W. Barsoum, Evidence for bulk ripplocations in layered solids, Sci. Rep. **6**, 33451 (2016).

[18] M. W. Barsoum and G. J. Tucker, Deformation of layered solids: Ripplocations not basal dislocations, Scr. Mater. **139**, 166 (2017).

[19] D. Freiberg, M. W. Barsoum, and G. J. Tucker, Nucleation of ripplocations through atomistic modeling of surface nanoindentation in graphite, Phys. Rev. Mater. **2**, 053602 (2018).

[20] J. Aslin, E. Mariani, K. Dawson, and M. W. Barsoum, Ripplocations provide a new mechanism for the deformation of phyllosilicates in the lithosphere, Nat. Commun. **10**, 686 (2019).

[21] A. V. Alaferdov, R. Savu, M. A. Canesqui, Y. V. Kopelevich, R. R. da Silva, N. N. Rozhkova, D. A. Pavlov, Y. V. Usov, G. M. de Trindade, and S. A. Moshkalev, Ripplocation in graphite nanoplatelets during sonication assisted liquid phase exfoliation, Carbon N.Y. **129**, 826 (2018).

[22] A. K. Kronenberg, S. H. Kirby, and J. Pinkston, Basal slip and mechanical anisotropy of biotite, J. Geophys. Res. **95**, 19257 (1990).

[23] B. Budiansky, N. A. Fleck, and J. C. Amazigo, On kink-band propagation in fiber composites, J. Mech. Phys. Solids. **46**, 1637 (1998).

[24] Q. Yang and B. Cox, Cohesive models for damage evolution in laminated composites, Int. J. Fract. **133**, 107 (2005).

[25] N. A. Fleck, Compressive failure of fiber composites, Adv. Appl. Mech. **33**, 43 (1997).

[26] G. W. Bentzel, M. Sokol, J. Griggs, A. C. Lang, and M. W. Barsoum, On the interactions of $Ti_2AlC$, $Ti_3AlC_2$, $Ti_3SiC_2$ and $Cr_2AlC$ with palladium at 900 °C, J. Alloys Compd. **771**, 1103 (2019).

[27] M. W. Barsoum, T. Zhen, S. R. Kalidindi, M. Radovic, and A. Murugaiah, Fully reversible, dislocation-based compressive deformation of $Ti_3SiC_2$ to 1 GPa, Nat. Mater. **2**, 107 (2003).

[28] A. G. Zhou and M. W. Barsoum, Kinking nonlinear elastic deformation of $Ti_3AlC_2$, $Ti_2AlC$, $Ti_3Al(C_{0.5}, N_{0.5})2$ and $Ti_2Al(C_{0.5}, N_{0.5})$, J. Alloys Compd. **498**, 62 (2010).

[29] S. Basu, A. Zhou, and M. W. Barsoum, On spherical nanoindentations, kinking nonlinear elasticity of mica single crystals and their geological implications, J. Struct. Geol. **31**, 791 (2009).

[30] R. Bhattacharya, R. Benitez, M. Radovic, and N. C. Goulbourne, High strain-rate response and deformation mechanisms in polycrystalline $Ti_2AlC$, Mater. Sci. Eng. A **598**, 319 (2014).

[31] P. Naik Parrikar, H. Gao, M. Radovic, and A. Shukla, Static and dynamic thermo-mechanical behavior of $Ti_2AlC$ MAX phase and fiber reinforced $Ti_2AlC$ composites, *Dynamic Behavior of Materials*, Conference Proceedings of the Society for Experimental Mechanics Series book series (CPSEMS) (Springer, Cham, 2015), Vol. 1, pp. 9–14.

[32] P. Naik Parrikar, R. Benitez, H. Gao, M. Radovic, and A. Shukla, Mechanical response of fine grained $Ti_2AlC$ under extreme thermo-mechanical loading conditions, Mater. Sci. Eng. A **658**, 176 (2016).

[33] L. Shannahan, M. W. Barsoum, and L. Lamberson, Dynamic fracture behavior of a MAX phase $Ti_3SiC_2$, Eng. Fract. Mech. **169**, 54 (2017).

[34] J. L. Jordan, Hugoniot Measurements of High Pressure Phase Stability of Titanium-silicon Carbide ($Ti_3SiC_2$), *AIP Conf. Proc.* 706 (AIP, New York, 2004), p. 77.

[35] L. M. Barker and R. E. Hollenbach, Laser interferometer for measuring high velocities of any reflecting surface, J. Appl. Phys. **43**, 4669 (1972).

[36] W. S. Rasband and ImageJ, U.S. National Institutes of Health, Bethesda, MD, 1997–2005, (n.d.), http://rsb.info.nih.gov/ij/.

[37] M. Radovic, M. W. Barsoum, A. Ganguly, T. Zhen, P. Finkel, S. R. Kalidindi, and E. Lara-Curzio, On the elastic properties and mechanical damping of $Ti_3SiC_2$, $Ti_3GeC_2$, $Ti_3Si_{0.5}Al_{0.5}C_2$ and $Ti_2AlC$ in the 300–1573 K temperature range, Acta Mater. **54**, 2757 (2006).

[38] E. B. Zaretsky, High temperature impact response of 998 alumina, J. Appl. Phys. **114**, 183518 (2013).

[39] L. M. Barker and R. E. Hollenbach, Shock-wave studies of PMMA, fused silica, and sapphire, J. Appl. Phys. **41**, 4208 (1970).

[40] D. J. Chapman, D. E. Eakins, D. M. Williamson, and W. Proud, *Index of Refraction Measurements and Window Corrections for PMMA Under Shock Compression*, AIP Conf. Proc. No. 1426 (AIP, New York, 2012), pp. 442–445.

[41] I. Girlitsky, E. Zaretsky, S. Kalabukhov, M. P. Dariel, and N. Frage, Dynamic compressive and tensile strengths of spark plasma sintered alumina, J. Appl. Phys. **115**, 243505 (2014).

[42] G. I. Kanel, V. E. Fortov, and S. V. Razorenov, *Shock-Wave Phenomena and the Properties of Condensed Matter* (Springer, New York, 2004).

[43] M. W. Barsoum and T. El-Raghy, Synthesis and characterization of a remarkable ceramic: $Ti_3SiC_2$, J. Am. Ceram. Soc. **79**, 1953 (1996).

[44] T. El-Raghy, M. W. Barsoum, A. Zavaliangos, and S. R. Kalidindi, Processing and mechanical properties of $Ti_3SiC_2$: II, Effect of grain size and deformation temperature, J. Am. Ceram. Soc. **82**, 2855 (2004).

[45] Y. Bao, H. Zhang, and Y. Zhou, Punch-shear tests and size effects for evaluating the shear strength of machinable ceramics, Z. Met. **95**, 372 (2004).

[46] M. W. Barsoum, D. Brodkin, and T. El-Raghy, Layered machinable ceramics for high temperature applications, Scr. Mater. **36**, 535 (1997).

[47] G. E. Duvall and R. A. Graham, Phase transitions under shock-wave loading, Rev. Mod. Phys. **49**, 523 (1977).

[48] B. Escaig, Dissociation and mechanical properties. Dislocation splitting and the plastic glide process in crystals, J. Phys. Colloq. **35**, C7–151 (1974).

[49] B. Manoun, S. K. Saxena, H. -P. Liermann, and M. W. Barsoum, Thermal expansion of polycrystalline $Ti_3SiC_2$ in the 25°–1400 °C temperature range, J. Am. Ceram. Soc. **88**, 3489 (2005).

[50] R. Fowles and R. F. Williams, Plane stress wave propagation in solids, J. Appl. Phys. **41**, 360 (1970).

[51] E. B. Zaretsky, G. I. Kanel, S. V. Razorenov, and K. Baumung, Impact strength properties of nickel-based refractory superalloys at normal and elevated temperatures, Int. J. Impact Eng. **31**, 41 (2005).

[52] A. V. Antoun, T. Seaman, L. Curran, D. R. Kanel, G. I. Razorenov, and S. V. Utkin, *Spall Fracture* (Springer, New-York, 2002).

[53] M. W. Barsoum, *MAX Phases Properties of Machinable Ternary Carbides and Nitrides*, 1st ed. (Wiley, Weinheim, Germany, 2013).

[54] G. E. Duvall, *Propagation of Plane Shock Waves in a Stress-Relaxing Medium, in: Stress Waves Anelastic Solids* (Springer, Berlin, 1964), pp. 20–32.

[55] A. D. Brailsford, Anharmonicity contributions to dislocation drag, J. Appl. Phys. **43**, 1380 (1972).

[56] C. S. Alexander, L. C. Chhabildas, W. D. Reinhart, and D. W. Templeton, Changes to the shock response of fused quartz due to glass modification, Int. J. Impact Eng. **35**, 1376 (2008).

[57] D. E. Munson and R. J. Lawrence, Dynamic deformation of polycrystalline alumina, J. Appl. Phys. **50**, 6272 (1979).

[58] D. R. Christman and N. H. Fnoulaf, Dynamic properties of high-purity beryllium, AIAA J. **8**, 477 (1970).

[59] S. V. Razorenov, *Hugoniot Elastic Limit and Spall Strength of Aluminum and Copper Single Crystals over a Wide Range of Strain Rates and Temperatures*, AIP Conf. Proc. No. 503 (AIP, New York, 2003).

[60] M. E. Kipp and D. E. Grady, Shock compression and release in high-strength ceramics, Technical Report No. SAND-89-1461, Albuquerque, NM, and Livermore, CA (1989).

[61] C. H. Mok and J. Duffy, The dynamic stress-strain relation of metals as determined from impact tests with a hard ball, Int. J. Mech. Sci. **7**, 355 (1965).

[62] M. Sokol, S. Kalabukhov, R. Shneck, E. Zaretsky, and N. Frage, Effect of grain size on the static and dynamic mechanical properties of magnesium aluminate spinel ($MgAl_2O_4$), J. Eur. Ceram. Soc. **37**, 3417 (2017).

[63] E. B. Zaretsky and G. I. Kanel, The high temperature impact response of tungsten and chromium, J. Appl. Phys. **122**, 115901 (2017).

[64] S. Asgari, E. El-Danaf, S. R. Kalidindi, and R. D. Doherty, Strain hardening regimes and microstructural evolution during

large strain compression of low stacking fault energy fcc alloys that form deformation twins, Metall. Mater. Trans. A **28**, 1781 (1997).

[65] M. H. Rice, R. G. McQueen, and J. M. Walsh, Compression of solids by strong shock waves, Solid State Phys. **6**, 1 (1958).

[66] G. I. Kanel, E. B. Zaretsky, S. V. Razorenov, A. S. Savinykh, and G. V. Garkushin, *Evolutions of Elastic-plastic Shock Compression Waves in Different Materials*, AIP Conf. Proc. 1793 (AIP, New York, 2017), p. 100030.

[67] E. B. Zaretsky and G. I. Kanel, Effect of temperature, strain, and strain rate on the flow stress of aluminum under shock-wave compression, J. Appl. Phys. **112**, 073504 (2012).

[68] E. B. Zaretsky and G. I. Kanel, Response of copper to shock-wave loading at temperatures up to the melting point, J. Appl. Phys. **114**, 083511 (2013).